GSC Advanced Research and Reviews
eISSN: 2582-4597 CODEN (USA): GARRC2
Cross Ref DOI: 10.30574/gscarr
Journal homepage: https://gscarr.gsconlinepress.com/

(RESEARCH ARTICLE)

Check for updates

INTERANNUAL RECURRENCE OF SATELLITE-OBSERVED FORMALDEHYDE TRANSITIONS AND SEASONALLY STRUCTURED, COORDINATED MULTIPOLLUTANT SHIFTS AT A TROPICAL URBAN FOREST–CITY INTERFACE IN WEST AFRICA (2024–2026)

Aka Jacques Adon [1,*], Guebi Daniel Akagbo [1], Véronique Yoboué [2] and Aristide Akpo [3]

[1] Laboratory of Fundamental and Applied Physics, Faculty of Fundamental and Applied Sciences (UFR SFA), Nangui Abrogoua University, 02 BP 801 Abidjan 02, Côte d'Ivoire
[2] Laboratory of Atmospheric Physics, Faculty of Sciences of the Structures of Matter and Technology (UFR SSMT), Félix Houphouët-Boigny University, BPV 34 Abidjan, Côte d'Ivoire
[3] Laboratory of Radiation Physics, Faculty of Sciences and Techniques (FAST), University of Abomey-Calavi, Cotonou, Benin
* Corresponding Author; Email: adonjacks1@gmail.com

ORCID Details
Aka Jacques Adon: https://orcid.org/0009-0006-4979-6494

GSC Advanced Research and Reviews, 2026, 29(02), 021–040

Publication history: Received on 25 August 2026; revised on 28 October 2026; accepted on 30 October 2026

Article DOI: https://doi.org/10.30574/gscarr.2026.29.2.0290

Copyright © 2026 Author(s) retain the copyright of this article. This article is published under the terms of the Creative Commons Attribution License 4.0

ABSTRACT

Forest–city interfaces combine biogenic, urban and regional combustion influences under strong seasonality. We test whether recurrent 2024–2026 tropospheric HCHO transitions at the Banco forest–metropolis interface in Abidjan are accompanied by coordinated multipollutant shifts, and whether such shifts can be separated from the seasonal cycle. The change points fall on 9 March 2024, 13 April 2025 and 13 April 2026, all within the long rainy season. The primary PCA uses the HCHO–NO_2–tropospheric-O_3 block on 441 complete-case dates; a five-species PCA adding CO and SO_2 is complementary because their extraction chain cannot be fully certified. Primary PC1 explains 54.1 % of variance, with loadings +0.861 (HCHO), +0.821 (NO_2) and −0.456 (O_3), and its raw transition contrasts are −1.416, −1.737 and −1.368 in 2024–2026. After categorical seasonal adjustment, without refitting the PCA, these contrasts become +0.026, −0.409 and −0.188; only the 2025 residual decrease remains robust across block lengths. Under a pre-specified harmonic adjustment, no primary residual contrast is robust in any year on either the 441-date or the 487-date support, while raw contrasts remain robust. HCHO–NO_2 covariance remains robust across block lengths after categorical seasonal adjustment ($\rho = 0.267$; within-year block bootstrap). The evidence supports recurrent, strongly seasonally structured coordinated multipollutant shifts. Categorical and harmonic seasonal representations diverge, consistent with transitions recurring at similar calendar dates; a season-independent component therefore cannot be robustly isolated from three years of data, which does not establish that none exists. No source attribution is made, and the primary inference does not rely on CO/SO_2.

Keywords: HCHO; NO_2; CO; Tropospheric O_3; Air Pollution; Multipollutant Covariance; Hydro-Meteorology; Fires; Banco; Abidjan; West Africa.

1 INTRODUCTION

Biogenic and anthropogenic volatile organic compounds (VOCs) contribute to oxidative tropospheric chemistry and to the formation of ozone and secondary organic aerosols. Biogenic emissions respond in particular to temperature, radiation, vegetation state, and water stress (Guenther et al., 2012), while VOC–NO_x–O_3 chemistry is intrinsically nonlinear and scale dependent (Monks et al., 2015). Formaldehyde (HCHO), an intermediate product of the oxidation of many VOCs, therefore provides an integrated satellite signal of VOC oxidation rather than a source-specific measurement. Historical and recent African and global applications confirm the value of HCHO for constraining VOC emissions, while emphasizing the contribution of multi-species constraints and models for quantitative attribution (Marais et al., 2012; Opacka et al., 2025; Sfendla et al., 2026).

International studies use satellite HCHO in complementary ways: HCHO–NO_2 constraints with inverse modelling over Africa (Opacka et al., 2025), TROPOMI HCHO/NO_x assimilation for NMVOC and ozone analysis in China (Feng et al., 2024), top-down VOC inversion with ground validation in Europe (Oomen et al., 2024), and satellite–ground HCHO evaluation in Australia/New Zealand (Ryan et al., 2020). Studies based on the HCHO/NO_2 column ratio (hereafter FNR) further show that this ratio is informative but sensitive to meteorology, transport and spatial representativeness (Schroeder et al., 2017; Souri et al., 2023; Johnson et al., 2023). These approaches motivate a conservative Banco analysis centred on recurrent covariance rather than source inversion or categorical ozone-regime attribution.

Previous satellite studies have already related HCHO variability to co-occurring atmospheric species, meteorological conditions, vegetation, and fire activity. In particular, Dhankar and Pani (2025) analysed TROPOMI HCHO together with CO, NO_2, land-surface temperature, precipitation, fire radiative power, and enhanced vegetation index over Southeast Asia. The unresolved question addressed here is therefore not whether such associations exist, but whether objectively detected HCHO transitions recur across consecutive annual records at a protected forest–metropolis interface and whether the accompanying coordinated multipollutant shifts remain identifiable under temporal, compositional, and seasonal sensitivity analyses, including whether they can be separated from the seasonal cycle.

In southern West Africa, the DACCIWA programme established a regional observational framework for investigating interactions among anthropogenic emissions, atmospheric composition, meteorology, and the West African monsoon (Knippertz et al., 2015). Source-oriented measurements subsequently conducted in Abidjan and Cotonou documented the complex mixture of combustion-related urban emissions characteristic of rapidly growing coastal environments (Adon et al., 2020). This regional evidence provides an important observational context for interpreting Banco as a forest–metropolis interface rather than as an isolated tropical site.

Banco National Park provides a particularly relevant setting in which to examine this complexity. This protected evergreen tropical forest, covering approximately 3,474 ha, is embedded within the Abidjan agglomeration. The forest–metropolis interface therefore creates a situation in which vegetation emissions, urban activities, combustion, and regional transport may overlap. The objective is not to assume that any one of these terms dominates, but to examine how their shared atmospheric environment is organized over time.

The Banco HCHO record itself displays a strong intra-annual organization, with recurrent transitions between 2024 and 2026, associations with hydro-meteorological conditions—particularly antecedent rainfall—and, in 2024–2025, positive covariance with regional fire activity. These features are re-derived here from the harmonized record (Sections 3.1, 3.7 and 3.8) rather than imported as established prior knowledge. Taken alone, however, they cannot determine whether HCHO behaves as an isolated signal or is accompanied by coordinated shifts in other atmospheric species. This question motivates the multipollutant extension developed below.

This extension reframes the scientific question. Rather than attempting to attribute HCHO variations directly to a specific source, we test whether its recurrent transitions are embedded in a covariance structure involving other atmospheric species and whether this structure converges with a coherent hydro-meteorological context. Particular attention is given to NO_2 and, in a complementary analysis, CO, which may provide additional information on the chemical environment, and to tropospheric O_3, treated as a descriptor of the regional photochemical context rather than as a surface-ozone measurement.

Throughout this study, statistical association, covariance, and coordinated multipollutant shifts are interpreted descriptively. A coordinated multipollutant shift denotes a common displacement of daily values along a covariance axis estimated over the whole record; it does not imply that the covariance structure itself differs before and after a transition, which is not tested here. Correlation, principal component analysis, change-point comparisons, and the targeted transport-feasibility pilot are not source-apportionment methods; source-specific interpretations therefore require independent constraints beyond the present observational design.

The central question is therefore: to what extent are the recurrent HCHO transitions observed between 2024 and 2026 over the Banco forest–metropolis interface accompanied by coordinated shifts of the primary HCHO–NO_2–O_3 block and by hydro-meteorological modulation, to what extent can these shifts be distinguished from the seasonal cycle, and to what extent do complementary chemical and fire indicators broaden this context without constituting source attribution?

2 MATERIALS AND METHODS

2.1 Study area and seasonal framework

The study focuses on the Banco National Park sector in Abidjan, Côte d'Ivoire, located approximately between 5°21′–5°25′ N and 4°01′–4°05′ W (Figure 1). The regional climate is tropical subequatorial. The seasonal framework used for the multipollutant analysis distinguishes the long dry season (December–February), the long rainy season (March–June), the short dry season (July–August), and the short rainy season (September–November). The common multipollutant comparison window is restricted to 1 January–8 August for 2024, 2025, and 2026.

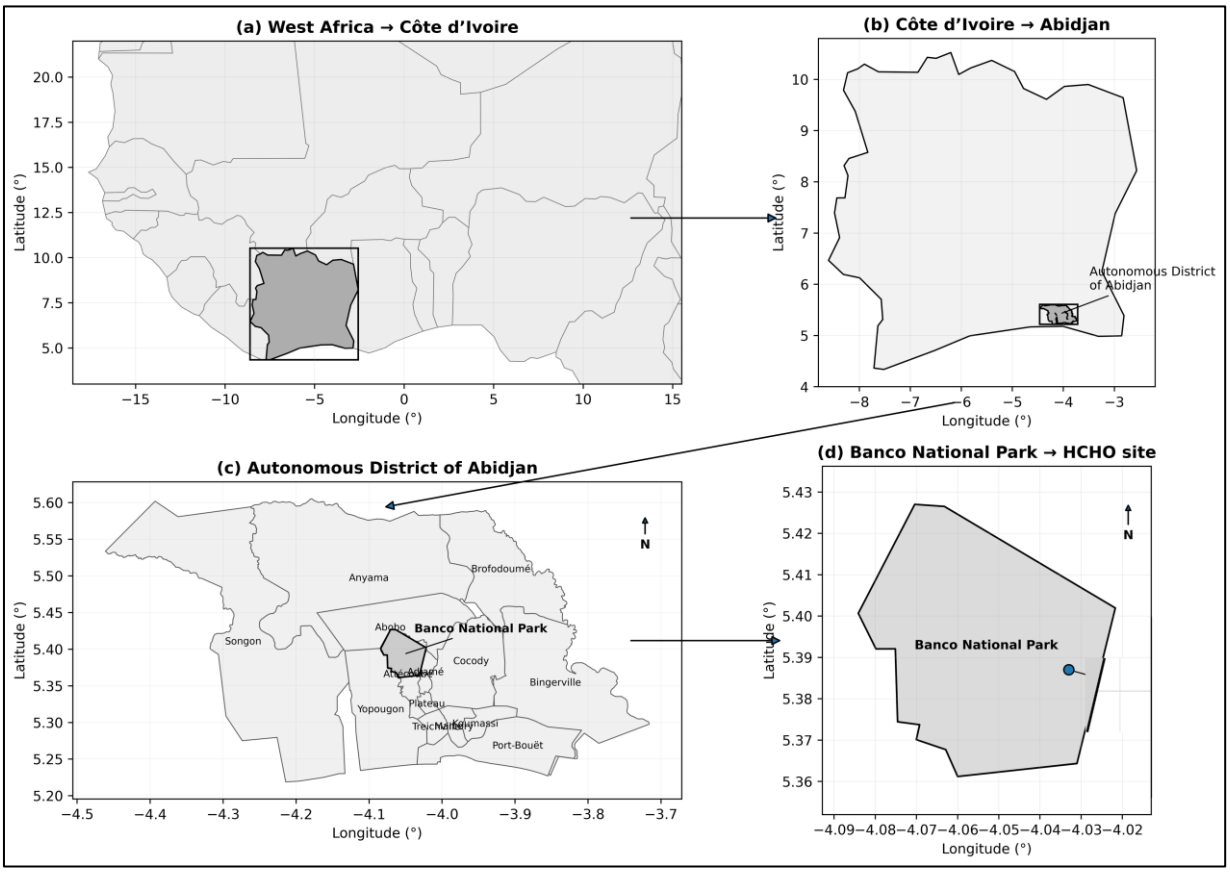


Figure 1: Geographic setting of Banco National Park in Abidjan, Côte d'Ivoire, West Africa. (a) Location of Côte d'Ivoire within West Africa; (b) location of the Autonomous District of Abidjan within Côte d'Ivoire; (c) administrative subdivisions of Abidjan and location of Banco National Park; and (d) detailed location of Banco National Park and the Banco-HCHO observation point used for change-point estimation. Arrows indicate successive geographic enlargements from the regional to the local scale. Administrative boundaries for the 14 subdivisions of Abidjan are based on OpenStreetMap and geoBoundaries data; the Banco National Park boundary follows a generalized outline retaining principal vertices, traceable to Decree 2018-510/OIPR.

2.2 HCHO and intra-annual transitions

Tropospheric HCHO used for change-point estimation (hereafter Banco-HCHO) is derived from Sentinel-5P/TROPOMI (Veefkind et al., 2012), using the COPERNICUS/S5P/OFFL/L3_HCHO collection and the tropospheric_HCHO_column_number_density variable; direct validation of the TROPOMI HCHO retrieval and its uncertainties is documented, in particular, by De Smedt et al. (2021). Change points are located using the nonparametric Pettitt test (Pettitt, 1979), applied to n = 135, 108 and 143 valid HCHO observations for 2024, 2025 and 2026, respectively. The Pettitt statistic is $K = \max |U_t|$ with $U_t = 2 \sum_{i=1}^{t} R_i - t(n + 1)$, evaluated over t = 1 to n − 1, where R_i is the rank of the i-th observation in the annual series. Inference uses contiguous disjoint blocks of length L, with the

terminal partial block retained; block order is permuted and the observed K is compared with the permuted K values. The one-sided empirical p-value is (r + 1)/(B + 1) with B = 5,000 per block length, so the minimum attainable value is 2.0×10^{-4}. Significance is assessed at $\alpha = 0.05$ for each L separately, and a transition is described as robust only when $p < 0.05$ for every tested L. Block lengths are L = 3, 5, 7, 10 and 14 valid observations. Location intervals are obtained using residual block bootstrap conditional on a two-segment model, with 3,000 replications for each L. The resulting central dates are used as descriptive boundaries for the multipollutant comparison across the estimated transition, with the estimates and 95 % location envelopes presented in Section 3.1.

2.3 Multipollutant chemical block

A separate multipollutant extraction combines HCHO, tropospheric NO_2, and tropospheric O_3 on 487 strictly common dates between 2024 and 2026, over the common 1 January–8 August window. NO_2 is represented by the Sentinel-5P/TROPOMI OFFL tropospheric column (tropospheric_NO_2_column_number_density; van Geffen et al., 2022). O_3 is derived from the O3_TCL Convective Cloud Differential (CCD) product, which in the tropics represents a clear-sky partial column from the surface to 270 hPa; each daily field corresponds to a three-day moving average. O_3 is therefore treated as a descriptor of the regional photochemical context and not as surface ozone or as an observation spatially co-resolved with HCHO and NO_2. Daily values are matched by date without imputation. These three species constitute the primary multivariate block: they define the VOC–NO_x–O_3 context and the FNR, and their source products and retrieval variables are documented above. Their historical extraction is nonetheless only partly documented, because the O_3 extraction parameters and the original multi-gas extraction script were not recovered (Section 7). CO and SO_2 values, held in the separate matched daily table ((see Data availability and reproducibility)), are used only in a complementary five-species PCA. An archived Google Earth Engine script documents Sentinel-5P OFFL/L3 CO and SO_2 collections and the CO_column_number_density and SO2_column_number_density fields, with a 25-km Abidjan buffer and 7,000-m reduction scale for its daily export; however, the corresponding historical numerical export has not been recovered and authenticated against the CO/SO_2 values in the present PCA. The script is therefore not treated as proof of the exact historical extraction chain, and no unrecovered QA threshold or extraction parameter is reconstructed retrospectively.

The HCHO series used in the multipollutant block (hereafter Matched-HCHO) is not interchangeable with the historical Banco series used for change-point estimation (Banco-HCHO). The two differ in extraction geometry and reduction scale: Banco-HCHO is extracted on the historical Banco geometry described in Section 2.2, whereas Matched-HCHO is extracted over the multi-gas Abidjan buffer, using a Sentinel-5P reduction scale of 7,000 m. The multi-gas extraction was performed using a 25-km-radius buffer. The manuscript record gives a buffer centre of 5.35995° N, 4.0083° W, whereas an archived re-export script records 5.3528° N, 4.0171° W (approximately 1.3 km apart). The original Earth Engine extraction script needed to resolve this coordinate discrepancy was not recovered. This discrepancy does not affect the certified matched dataset used in the analyses. The Banco-HCHO observation point (5.387° N, 4.033° W; Figure 1d) lies approximately 4 km from either candidate centre and therefore well inside the buffer. Over the same 1 January–8 August window, the two supports retain different numbers of valid daily observations: 135, 108 and 143 for Banco-HCHO and 159, 167 and 161 for Matched-HCHO in 2024, 2025 and 2026, respectively. Change points are estimated on Banco-HCHO (Section 2.2) and the multipollutant axis is built on Matched-HCHO; the consequences of this distinction are examined in Sections 2.6 and 3.4. This dual-support design was retained because Banco-HCHO preserves the historical site-specific series used for transition detection, whereas Matched-HCHO provides the common temporal and spatial support required for the multipollutant comparison; sensitivity analyses explicitly test whether this support distinction affects the central inference. The TROPOMI NO_2 retrieval framework and the version v2.2 retrieval improvements are documented by van Geffen et al. (2022).

The tropospheric O_3 product used in the matched block is smoothed over three days; daily p-values involving O_3 are therefore reported as descriptive diagnostics and are not interpreted as tests based on temporally independent observations.

2.4 Correlations, seasonal adjustment, and FNR

Chemical associations are quantified using Spearman correlations. To assess the role of shared seasonality, each variable is rank transformed and then categorically adjusted for the seasons present within the common window—the long dry season, long rainy season, and short dry season—and the adjusted associations correspond to correlations between rank residuals. Holm correction (Holm, 1979) is applied separately within the raw family and the season-adjusted family, each comprising the same three pair tests: HCHO–NO_2, HCHO–O_3 and NO_2–O_3. Parametric tests of the raw family use n − 2 degrees of freedom, whereas those of the season-adjusted family use n − 2 − (k − 1) with k = 3 season categories, because the three-level categorical adjustment introduces two independent indicator contrasts. Because the rank residuals are serially dependent, these parametric p-values are reported as secondary descriptors only, and the primary inference for the chemical pairs is a moving-block bootstrap. Blocks are resampled within each calendar year, so that no block crosses a year boundary, and they run over successive available observations rather than successive calendar days; no absent day is reconstructed or imputed. Block lengths L = 3, 5, 7, 10 and 14 are used with 5,000 replications, and an association is described as robust only when the 95 % interval excludes zero at every tested

block length. FNR is defined as $HCHO/NO_2$. Negative HCHO values are not silently censored; positive-only sensitivity analyses and analyses excluding the lowest NO_2 columns are retained. Interannual comparison of FNR is based on a Kruskal–Wallis test (Kruskal & Wallis, 1952). No universal VOC-limited/NO_x-limited threshold is imported. Interpretation of FNR accounts for limitations related to column/boundary-layer representativeness, retrieval uncertainties, and chemical nonlinearity documented by Schroeder et al. (2017), Johnson et al. (2023), and Souri et al. (2023); recent studies further support the use of non-binary frameworks rather than universal thresholds (Tian et al., 2025; Souri et al., 2026).

2.5 Chemical principal component analysis

The primary chemical PCA is the standardized HCHO–NO_2–tropospheric O_3 analysis on the 441-date common support already used for the composition sensitivity comparisons. Component signs are oriented so that the HCHO loading is positive. Loadings are interpreted as variable–component correlations, and components describe structures of chemical covariance rather than source fractions. The three active variables do not share the same effective temporal resolution. HCHO and NO_2 enter the analysis as daily values, whereas each daily tropospheric O_3 field of the O3_TCL product represents a three-day moving average (Section 2.3). The covariance structure is therefore estimated between variables whose high-frequency variability is differently attenuated, and the O_3 loading on PC1 is interpreted in that light rather than as a like-for-like daily association. Variables entering the chemical PCAs were standardized using the population standard deviation (ddof = 0). A standardized five-species PCA adding CO and SO_2 on the same 441 complete cases is retained as a complementary compositional analysis, not as the primary axis. The general methodological framework for PCA follows Jolliffe and Cadima (2016).

2.6 Transition comparison and sensitivity analyses

For each year, PC1 scores are separated into two sequences according to the rule Pre = date ≤ HCHO change point and Post = date > HCHO change point. The statistic is ΔPC1 = mean(Post) − mean(Pre). Temporal robustness is evaluated using a moving-block bootstrap applied separately within the pre- and post-transition sequences, with 5,000 replications and block lengths L = 3, 5, 7, 10, and 14. A decrease in PC1 after the HCHO breakpoint is described as robust only when the 95 % confidence interval is entirely negative at every tested block length.

Complementary analyses test dependence on HCHO spatial support, inclusion of the transition-defining species, addition of CO and SO_2, seasonal structure, and arbitrary breakpoint placement. Change points were re-estimated on standardized Matched-HCHO within the 441-date comparison population (n = 145, 148 and 148 in 2024, 2025 and 2026), and the comparison across the estimated transition was repeated under both partitions. A no-HCHO PCA (NO_2, CO, tropospheric O_3 and SO_2) and the complementary five-species PCA were evaluated on the same 441 dates. For both the primary three-species PC1 and the complementary five-species PC1, categorical season effects were removed from the raw PC1 scores without refitting the PCA; residual scores were compared using the same year-specific HCHO change points and moving-block bootstrap (5,000 replications; L = 3, 5, 7, 10 and 14). Finally, an exhaustive circular-shift randomization was applied to each annual PC1 sequence of the complementary five-species axis. The observed Pre/Post label vector is shifted circularly by k = 0 to n − 1 positions, so that the reference set contains exactly n label assignments, the observed partition (k = 0) included; every assignment preserves the annual Pre/Post counts and keeps Pre as a single contiguous, wrapped block. The one-sided empirical p-value is the number of shifts whose ΔPC1 is less than or equal to the observed value, divided by n. The resolution of the test is therefore 1/n, and no p-value below 1/n is attainable. This is a randomization over a restricted set of n assignments rather than a general permutation test. Two conventions follow from the design and are stated for completeness: the circular shift makes the end and the beginning of each annual window adjacent, and positions are defined by successive available observations rather than successive calendar days, no missing day being reconstructed.

All axis comparisons use the same 441 dates: the HCHO–NO_2–O_3 PCA anchors the primary multivariate inference, the five-species axis evaluates added CO/SO_2 covariance, and the no-HCHO axis tests dependence on the transition-defining species.

To test whether the categorical season definition conditions the residual contrasts of the primary axis, a continuous seasonal-adjustment sensitivity was specified and frozen in a written protocol before the daily primary PC1 scores were accessed. Raw primary PC1 scores were taken unchanged from the archived 441-date and 487-date primary PCAs, without refitting either PCA, and the two supports were analysed separately. A seasonal cycle represented by annual harmonics of day of year (period 365.25 days) was fitted by least squares on the three years pooled and subtracted from the raw scores. The primary specification uses two harmonics (K = 2); K = 1, K = 3 and a leave-one-year-out variant, in which the two-harmonic cycle is fitted on the two other years and applied to the excluded year, are sensitivities. Residual contrasts were evaluated with the same change points, Pre/Post rule, moving-block bootstrap (5,000 replications; L = 3, 5, 7, 10 and 14) and robustness criterion as above, with a single analysis seed (see Data availability and reproducibility). The analysis script, finalized and tested on synthetic data before any run on the real scores, first verified the SHA-256 fingerprint of the input workbook and the sample sizes, and reproduced the reported raw ΔPC1

values to three decimals on both supports; it was designed to stop on any discrepancy. Because the change points fall at similar calendar dates in the three years, a smooth seasonal cycle can absorb part of the transition itself; this limitation was stated before the calculations, and the test therefore addresses the residual contrasts, not the existence of the transitions. The continuous sensitivity was applied to the primary axis only.

2.7 Hydro-meteorological and fire context

The environmental context uses ERA5 for maximum temperature (Hersbach et al., 2020), NASA POWER for relative humidity and solar radiation, CHIRPS for precipitation (Funk et al., 2015), and VIIRS/S-NPP for fire activity (Schroeder et al., 2014). A 7-day antecedent rainfall variable is derived. For fires, daily FRP values are aggregated within a local 0–100 km domain and a regional 100–250 km domain; a three-day moving accumulation (FRP3d) represents same-day and short-lag activity, and the analyses use ln(1 + FRP3d) to limit the influence of extreme values while retaining zero-FRP days. Two environmental PCAs are distinguished: a 2024–2026 analysis without FRP and a 2024–2025 analysis including fire indicators. Comparable 2026 FRP data are neither available, imputed, nor reconstructed.

The environmental analyses use analytical populations distinct from the matched chemical PCA. Starting from the 386 valid Banco-HCHO dates, the 2024–2026 environmental PCA retained 368 dates complete for the active environmental covariates, the losses arising from seven-day antecedent rainfall at the start of 2024 and, in 2026, from ERA5, CHIRPS and solar-radiation coverage ending on 30 June, so that the 2026 environmental analyses cover 1 January–30 June. The fire-inclusive PCA retained 239 observations, corresponding exactly to the 239 complete environmental-PCA dates from 2024–2025; 2026 was excluded by design because no comparable FRP series was available, and not through additional complete-case attrition.

In the environmental PCAs, HCHO is treated as a supplementary variable: it does not contribute to component construction and is projected a posteriori onto the environmental axes. Loadings are reported as variable–component correlations, as for the chemical PCAs (Section 2.5).

The main environmental inference relies on Spearman associations with confidence intervals obtained by block bootstrap and on the two complete-case environmental PCAs. These intervals are computed at a single block length (L = 7) and are therefore not evaluated against the multi-length robustness criterion applied to the chemical analyses (Section 2.4).

2.8 Wind, boundary-layer constraints, and targeted transport-feasibility pilot

ERA5 wind speed is treated as a sensitivity analysis because interannual coverage is not homogeneous. No homogeneous wind-direction series is available for Banco. A homogeneous daily PBLH series directly matched to the Banco record was not available for quantitative analysis over 2024–2026. Vertical dilution was therefore not tested quantitatively.

A targeted HYSPLIT–VIIRS pilot was run for one objectively high-HCHO event (6 February 2024): 72-h backward trajectories from the Banco transport reference location (5.392° N, 4.052° W) were initialized at 500, 1000 and 1500 m AGL at 10:00 UTC using GDAS1 meteorology and compared with VIIRS/S-NPP active fires within ±1 h using minimum haversine distance. This transport reference differs by approximately 2 km from the recovered Earth Engine HCHO point (5.387° N, 4.033° W) in Figure 1d, so the coordinates are retained as distinct archived analytical locations. The single-event pilot tests transport plausibility only, not source contribution or recurrent pyrogenic influence. Table 1 summarizes the analytical populations and sample sizes used across the study.

Table 1: Analytical populations and sample sizes used across the study.

Analysis	Analytical support	Period	N
Change-point detection	Banco-HCHO	2024	135
Change-point detection	Banco-HCHO	2025	108
Change-point detection	Banco-HCHO	2026	143
Matched chemical block	HCHO–NO_2–O_3 strict date matches (bivariate and FNR diagnostics)	2024–2026	487
Primary chemical PCA	HCHO, NO_2, O_3 on common comparison support	2024–2026	441
Primary chemical PCA, full matched population	HCHO, NO_2, O_3 on all strict date matches	2024–2026	487

Complementary five-species PCA	HCHO, NO_2, O_3, CO, SO_2 on common comparison support	2024–2026	441
No-HCHO composition axis	NO_2, CO, O_3, SO_2 on common comparison support	2024–2026	441
Individual-species composition controls	Standardized NO_2 and tropospheric O_3 on all strict date matches	2024–2026	487
Matched-HCHO breakpoint sensitivity	Common 441-date comparison population (annual n = 145 / 148 / 148)	2024–2026	441
Environmental PCA	Environmental covariates, without fires	2024–2026	368
Fire-inclusive environmental PCA	Environmental covariates + FRP	2024–2025	239

3 RESULTS

3.1 Recurrent HCHO transitions

Across 2024–2026, HCHO shows a recurrent shift from higher early-year levels toward lower values around April–May (Figure 2).

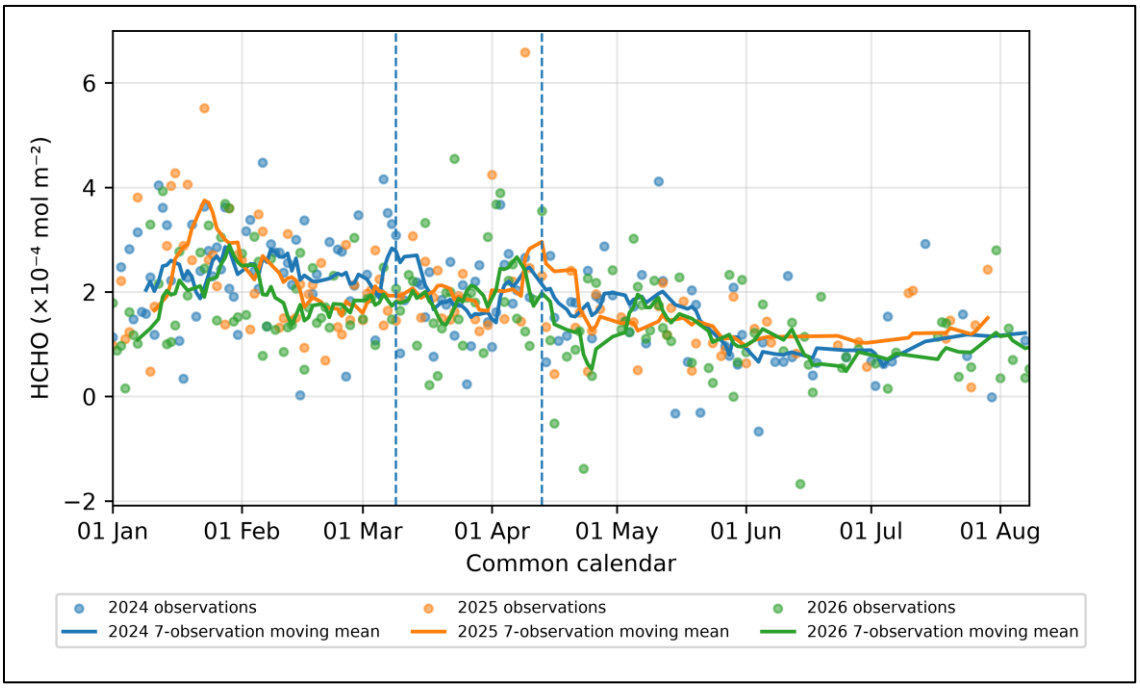


Figure 2: Harmonized daily Banco-HCHO observations over the common 1 January–8 August window. Dashed vertical lines indicate independently estimated raw change points (9 March 2024, 13 April 2025, and 13 April 2026); the 2025 and 2026 estimates coincide and therefore appear as a single overlapping line. Smoothed curves are 7-observation moving averages used for visualization only.

Central transition estimates are 9 March 2024, 13 April 2025 and 13 April 2026; their 95 % location envelopes are 15 February–28 March, 16 March–2 May and 22 March–2 May, respectively. The overlapping envelopes do not support statistically distinct annual transition calendars. The Pettitt statistics are K = 2,470 (2024), K = 1,532 (2025) and K = 2,506 (2026). Contiguous-block permutation p-values are 2.0×10^{-4}, 2.0×10^{-4}, 4.0×10^{-4}, 1.2×10^{-3} and 2.2×10^{-3} for 2024; 4.0×10^{-4}, 2.0×10^{-3}, 0.020, 0.013 and 0.057 for 2025; and 2.0×10^{-4}, 4.0×10^{-4}, 2.0×10^{-3}, 2.6×10^{-3} and 4.8×10^{-3} for 2026, at L = 3, 5, 7, 10 and 14 respectively. The transitions are therefore supported at every tested block length in 2024 and 2026. In 2025 the transition is supported at L = 3 to 10 but not at L = 14, where p = 0.057 with a Monte Carlo standard error of 0.003; 2025 is also the shortest record (n = 108), so L = 14 leaves only eight blocks, against ten in 2024 and eleven in 2026. The 2025 transition is consequently described as supported but not uniformly robust across block lengths. Mean Banco-HCHO columns decrease across the estimated transition from 2.430 to 1.487×10^{-4} mol m^{-2}

in 2024 (−38.8 %), from 2.225 to 1.289 × 10^{-4} mol m^{-2} in 2025 (−42.1 %), and from 1.922 to 1.068 × 10^{-4} mol m^{-2} in 2026 (−44.4 %). Thus, despite year-specific short-term variability, the principal temporal feature is a recurrent intra-annual downward transition whose multipollutant and hydro-meteorological context is examined below without assigning a single mechanism.

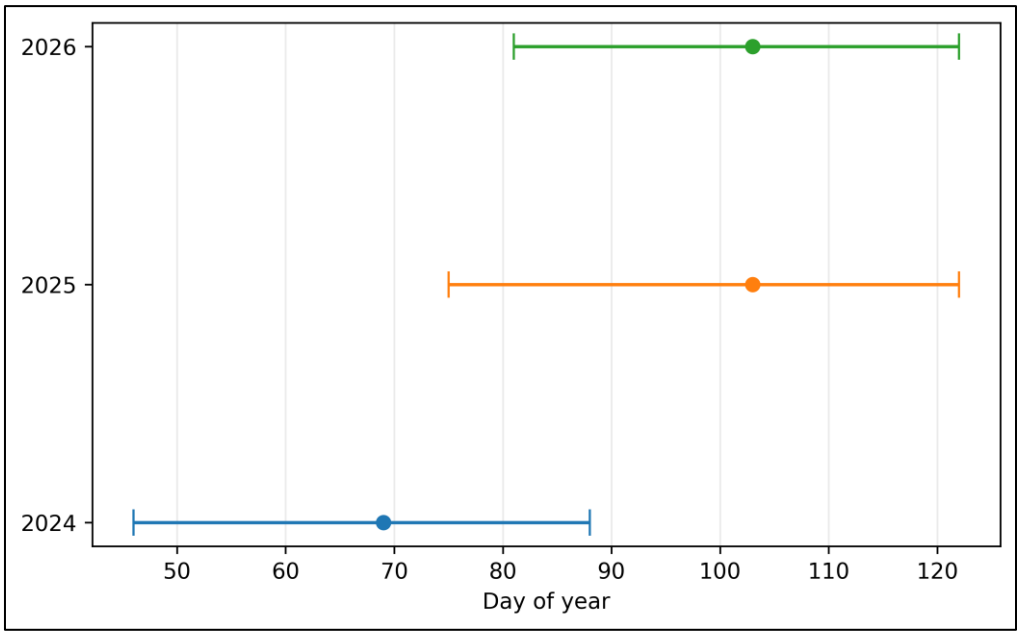


Figure 3: Raw change-point estimates and 95 % bootstrap location intervals obtained across the tested block lengths (L = 3–14). The substantial overlap indicates that the estimated transition timings are not statistically well separated.

Together, the central estimates and their overlapping location intervals support a recurrent seasonal transition window (Figure 3).

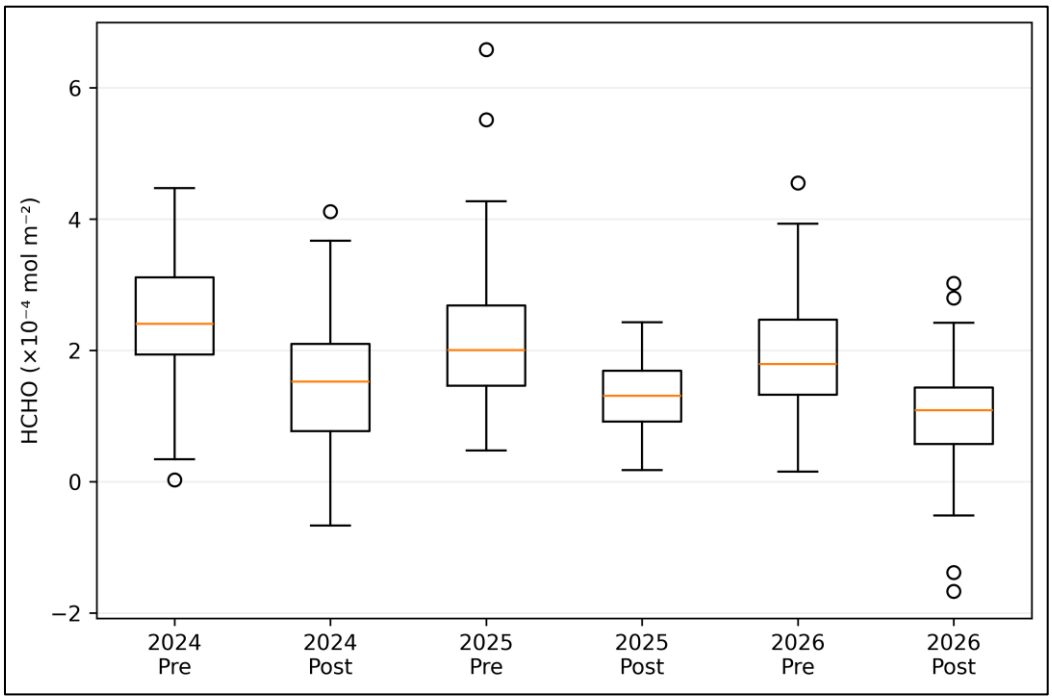


Figure 4: Banco-HCHO distributions before and after the intra-annual transition estimated independently for each year. All three years show a recurrent downward shift.

The pre- and post-transition distributions overlap partially in all three years (Figure 4): the recurrence is therefore distributional rather than a complete separation of two populations.

3.2 Multipollutant chemical structure

The matched dataset contains 487 HCHO–NO_2–O_3 dates. The 441-date support used below for every axis comparison is the five-species complete-case subset of those dates; the 46 excluded dates lack CO and/or SO_2. Restricting the primary three-species axis to this subset places all axis comparisons on an identical support, at the cost of a selection criterion defined by the availability of the complementary species; the full 487-date population is retained for the bivariate and FNR diagnostics. To assess this selection effect, the primary three-species PCA was also fitted to the full 487-date matched population. PC1 then explains 51.4 % of the variance and loads +0.840 on HCHO, +0.804 on NO_2 and −0.435 on tropospheric O_3. The raw post−pre ΔPC1 values are −1.366, −1.484 and −1.254 in 2024, 2025 and 2026, with moving-block bootstrap intervals entirely negative at every tested block length; after categorical seasonal adjustment the residual contrasts are +0.043, −0.304 and −0.162, with intervals including zero in 2024 and 2026 and entirely negative in 2025. The loadings, the direction of the transition contrast and its seasonal structuring are therefore preserved on the full 487-date support, although the raw contrasts are attenuated by 3.5 %, 14.6 % and 8.4 % relative to the 441-date support. These results indicate that the primary inference is robust to the complete-case restriction imposed by CO and SO_2 availability, although the magnitude of the transition contrast is attenuated on the full 487-date support. For direct composition comparisons, the primary three-species PCA is evaluated on the same 441-date support used by the complementary axis definitions. Its PC1 explains 54.1 % of the variance and loads +0.861 on HCHO, +0.821 on NO_2, and −0.456 on tropospheric O_3. The primary axis thus describes a dominant HCHO–NO_2 covariance mode opposed more weakly by tropospheric O_3, without being interpreted as a source factor.

The complementary five-species PCA adds CO and SO_2 to the same 441 dates. Its PC1 explains 43.4 % of the total variance and carries high positive loadings for HCHO (+0.876), CO (+0.835), and NO_2 (+0.778), with a weaker negative loading for O_3 (−0.318) (Figure 5). This extension shows that CO covaries with the dominant HCHO–NO_2 mode, but because the exact historical extraction chain of the archived CO/SO_2 values is not fully certified, the five-species PCA is used to characterize supplementary covariance structure rather than to anchor the primary multivariate inference. The proximity of HCHO, CO, and NO_2 must be interpreted as statistical co-organization, not as proof of a common source. Because the three-species and five-species PCAs have different dimensionality, their PC1 variance fractions (54.1 % and 43.4 %, respectively) are reported descriptively and are not directly comparable as measures of relative performance.

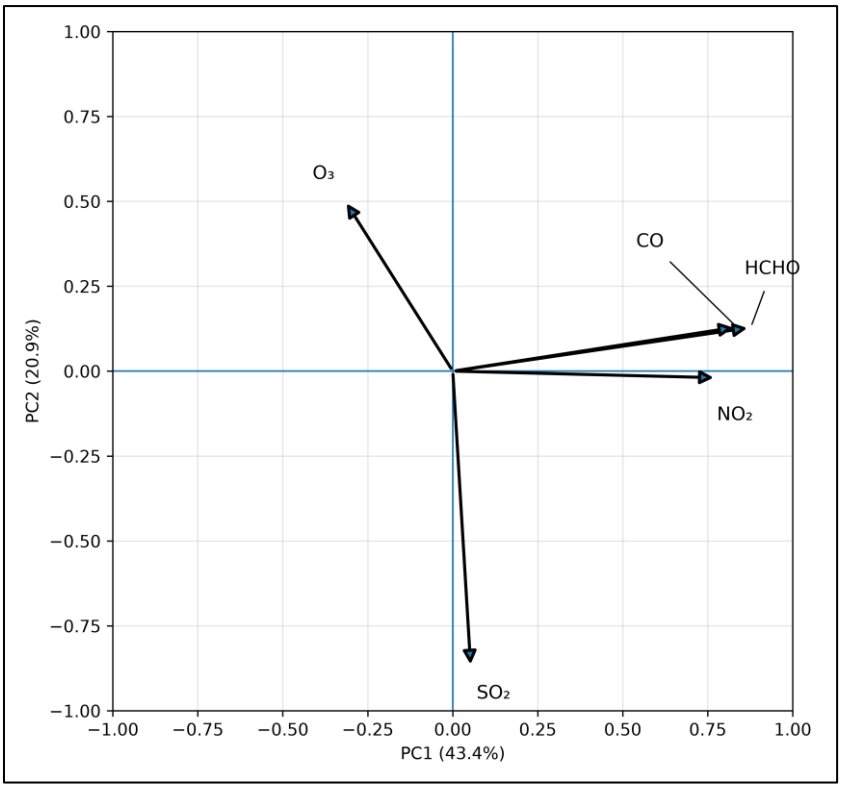


Figure 5: Complementary standardized five-species PCA for Matched-HCHO, NO_2, tropospheric O_3, CO, and SO_2 on 441 common dates. Vectors represent loadings on PC1 and PC2; PC1 explains 43.4 % of the variance and loads positively on HCHO (0.876), NO_2 (0.778), and CO (0.835), with a weaker negative O_3 loading (−0.318). This five-species representation is used as a compositional context; the primary multivariate inference is based on the primary HCHO–NO_2–O_3 PCA.

Within the complementary five-species PCA, tropospheric O_3 is opposed to the HCHO–CO–NO_2 triplet on PC1 and projects positively on PC2, while SO_2 contributes mainly to PC2. This configuration provides useful compositional context but does not identify chemical pathways or source fractions. The primary inference remains anchored to the primary HCHO–NO_2–O_3 axis.

3.3 HCHO–NO_2: covariance after categorical seasonal adjustment

The raw HCHO–NO_2 correlation is positive (ρ = 0.517). After categorical seasonal adjustment it remains detectable (ρ = 0.267), and the within-year block-bootstrap intervals exclude zero at every tested block length in both the raw and the adjusted form (Holm-corrected p = 3.81×10^{-34} and 7.36×10^{-9} respectively). The reduction in strength after adjustment shows that part of the signal is seasonal, but its persistence indicates that an HCHO–NO_2 covariance component is not fully reducible to the categorical seasonal calendar (Figure 6).

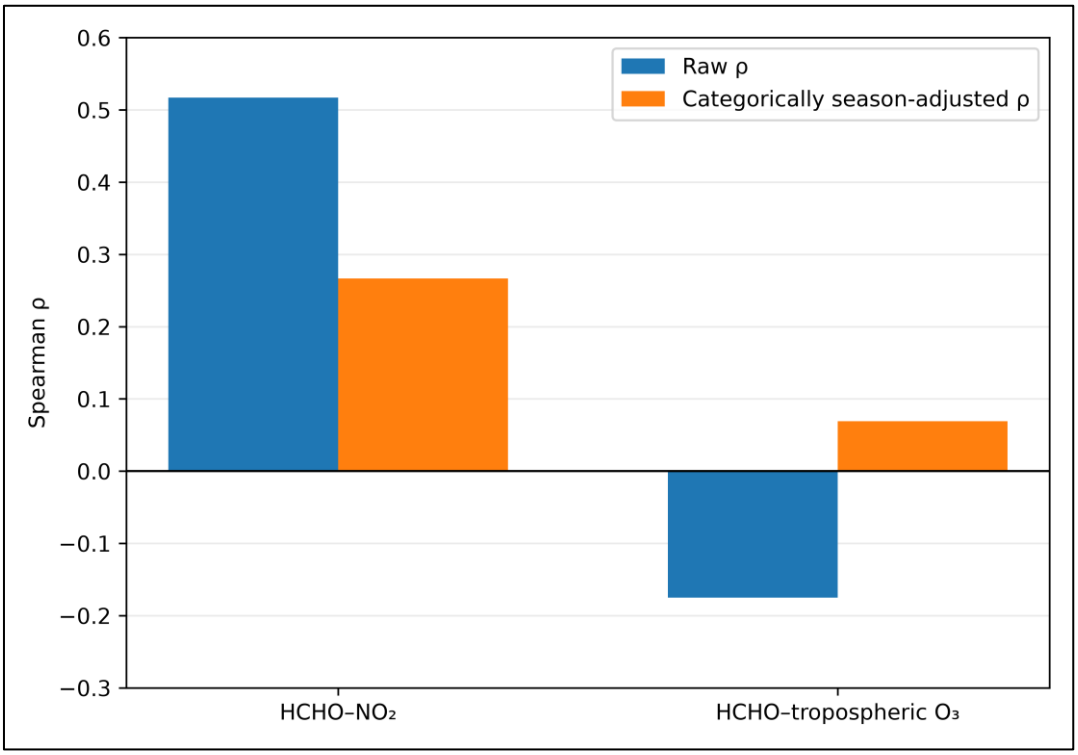


Figure 6: Covariance of HCHO–NO_2 and HCHO–tropospheric O_3 over 487 strictly matched dates, summarized by raw Spearman coefficients and coefficients categorically adjusted for seasonality. HCHO–NO_2 decreases from ρ = 0.517 to 0.267 after adjustment; HCHO–O_3 changes from −0.175 to 0.069.

The two pairs involving tropospheric O_3 behave differently. The raw HCHO–O_3 association is weakly negative (ρ = −0.175; Holm-corrected p = 2.04×10^{-4}), and its within-year block-bootstrap interval excludes zero at L = 3 and 5, lies practically at the zero boundary at L = 7 (upper bound −0.0007), and includes zero at L = 10 and 14, so the association is not robust across the full range; after adjustment it is weakly positive (ρ = +0.069; Holm-corrected p = 0.128) and is not robust at any tested block length. The raw NO_2–O_3 association is likewise weakly negative (ρ = −0.096; Holm-corrected p = 0.035) and becomes weakly positive after adjustment (ρ = +0.101; Holm-corrected p = 0.052), and neither form is robust at any tested block length. Seasonality therefore affects the three chemical pairs of the family differently, and HCHO–NO_2 is the only pair whose association is robust under dependence-aware inference.

3.4 Coordinated multipollutant shifts around HCHO transitions and sensitivity analyses

For the primary HCHO–NO_2–O_3 axis, the raw post–pre ΔPC1 values are −1.416, −1.737, and −1.368 in 2024, 2025, and 2026, respectively. After categorical seasonal adjustment of the raw primary PC1 scores without refitting the PCA, the corresponding residual contrasts are +0.026, −0.409, and −0.188. Moving-block bootstrap intervals include zero for all tested block lengths (L = 3, 5, 7, 10 and 14) in 2024 and 2026, whereas the 2025 residual decrease remains entirely negative across all tested block lengths. The primary transition contrast is therefore strongly seasonally structured, with a robust residual component detected in 2025 under categorical adjustment but not in 2024 or 2026. The complementary five-species axis yields raw differences of −1.987, −2.528, and −1.839, corresponding to mean Pre/Post scores of +1.313/−0.674 in 2024, +1.222/−1.306 in 2025 and +0.446/−1.393 in 2026. Its categorical seasonal adjustment attenuates those differences to −0.087, −0.941, and −0.394. After adjustment, the 2024 bootstrap intervals include zero for all tested block lengths; the 2025 intervals remain entirely negative for all block lengths; and the 2026

residual contrast remains negative but is not uniformly robust across block lengths. This five-species residual was assessed only under categorical adjustment; the continuous sensitivity reported below was not applied to this complementary axis, so it does not constitute an independent confirmation of a season-independent 2025 contrast. These robustness patterns concern different statistical questions and should not be directly compared. Section 3.1 tests the existence of a change point in the univariate Banco-HCHO record, whereas the analysis here tests whether a seasonally adjusted multipollutant contrast persists across an established partition on a different analytical support. The weaker block-permutation robustness of the 2025 Banco-HCHO change point therefore does not conflict with the stronger residual multipollutant contrast observed for that year under categorical adjustment, and no ranking of years from one analysis is transferred to the other.

The 2025 residual does not withstand continuous seasonal adjustment. On the 441-date support, the reproduced raw primary contrasts (−1.416, −1.737 and −1.368) become +0.061, −0.037 and +0.208 after removal of the two-harmonic cycle, and the 2025 bootstrap intervals include zero at every tested block length (L = 3: −0.361 to +0.199; L = 14: −0.522 to +0.208). The sensitivity variants give 2025 residuals of +0.067 (K = 1), −0.104 (K = 3) and −0.089 (leave-one-year-out), none of them robust. On the 487-date support, the reproduced raw contrasts (−1.366, −1.484 and −1.254) become +0.040, +0.036 and +0.194 under K = 2, and the 2025 residuals are +0.165, −0.031 and +0.038 under the three variants. No adjusted contrast satisfies the robustness criterion in any year, on either support or under any variant, and no adjusted interval excludes zero at every block length in either direction, whereas the raw contrasts remain robust on both supports. The 2026 residuals are positive under every continuous variant but are not robust and are not interpreted. Categorical and continuous adjustment therefore diverge for 2025: the residual decrease that is robust under the three-season partition is not distinguishable from the modelled smooth seasonal cycle. This divergence does not show that the categorical season boundaries produced the 2025 residual, and it does not affect the raw transition contrasts.

The common-support sensitivities confirm that the transition-associated decrease does not require CO or SO_2. Matched-HCHO change points yield five-species ΔPC1 values of −1.982, −2.709 and −1.863; excluding HCHO gives −1.407, −1.979 and −1.413; and the primary HCHO–NO_2–O_3 axis gives −1.416, −1.737 and −1.368 in 2024–2026, respectively (Table 2). In the exhaustive circular-shift randomization, the observed five-species decreases (−1.987, −2.528 and −1.839) lie in the negative tail of the year-specific randomization distributions, with one-sided empirical p = 0.0069, 0.0203 and 0.0068, corresponding to ranks 1 of 145, 3 of 148 and 1 of 148 among the admissible circular shifts. The 2024 and 2026 values are the minimum attainable at these sample sizes, 1/145 and 1/148, so for those two years the test can resolve the observed contrast no further than as the most extreme of the admissible shifts; the 2025 value is not at that floor.

This indicates that the transition contrasts of the complementary five-species axis occupy extreme ranks among the admissible circular shifts of that axis, under partitions of identical Pre/Post size. It does not extend to the primary axis, and it does not establish independence from seasonality.

The re-estimated partitions are reported explicitly because they are not equivalent to the primary ones. Change points re-estimated on the standardized Matched-HCHO column fall on 7 April 2024, 20 March 2025 and 7 April 2026. The 2025 and 2026 estimates lie within the 95 % location envelopes reported in Section 3.1, whereas the 2024 estimate falls beyond the 28 March upper bound. These alternative dates reassign 16.6 %, 10.1 % and 3.4 % of observations between Pre and Post; the largest reassignment and the only out-of-envelope date both occur in 2024, the year in which ΔPC1 changes least. When HCHO is excluded and the axis is recomputed from NO_2, CO, tropospheric O_3 and SO_2, PC1 explains 38.5 % of the variance, with loadings of +0.836 for NO_2, +0.817 for CO and −0.363 for O_3. Because this no-HCHO control necessarily includes CO and SO_2, it is reported as a composition sensitivity and not as an independent test of the primary analysis. A composition control free of both HCHO and the species whose historical extraction chain could not be fully authenticated was therefore evaluated on the full 487-date matched support. Standardized NO_2 decreases across the Banco-HCHO change points in all three years (Δ = −0.687, −1.062 and −0.586), with moving-block bootstrap intervals entirely negative at every tested block length; after categorical seasonal adjustment the contrasts are +0.129, −0.366 and +0.054, and only the 2025 decrease remains robust under that adjustment. Standardized tropospheric O_3 shows no robust raw contrast in any year (Δ = +0.146, −0.081 and +0.527), showing that the raw transition-associated decrease is not shared uniformly across the two independently tested species; its categorically adjusted 2025 contrast is, however, negative and robust (−0.540), whereas those of 2024 and 2026 are not. Neither of these 2025 composition-control residuals was submitted to the continuous harmonic adjustment applied to the primary axis (Section 2.6). Because NO_2 contains no HCHO and requires neither CO nor SO_2, this control shows that the decrease associated with the HCHO partitions is not carried exclusively by HCHO and does not depend on the uncertified extraction chain. The partition dates nevertheless remain derived from Banco-HCHO, and the control tests individual species rather than an independent multipollutant axis; it therefore does not by itself demonstrate a coordinated multipollutant shift independently of HCHO.

Table 2: Summary of transition sensitivity analyses (ΔPC1).

Year	Five-species axis	Without HCHO	Primary axis	Five-species, Matched-HCHO CP	Primary-axis 95 % CI envelope, L = 3–14
2024	−1.987	−1.407	−1.416	−1.982	−2.165 to −0.835
2025	−2.528	−1.979	−1.737	−2.709	−2.628 to −1.011
2026	−1.839	−1.413	−1.368	−1.863	−2.328 to −0.523

The second, third and fourth columns use the Banco-HCHO change points; the fifth uses the change points re-estimated on standardized Matched-HCHO (Section 3.4). The last column is the envelope of the five separate 95 % bootstrap intervals obtained at L = 3, 5, 7, 10 and 14 for the primary axis, that is the lowest lower bound and the highest upper bound across those block lengths; it is not a single aggregated interval, and each of the five intervals is entirely negative in every year.3.5. Tropospheric O_3: a distinct dimension.

3.5 Tropospheric O_3: a distinct dimension

Under dependence-aware inference, O_3 shows no association with either HCHO or NO_2 that is robust across the tested block lengths (Section 3.3), whereas HCHO–NO_2 remains robust in both raw and categorically adjusted form. O_3 is therefore retained as a tropospheric photochemical dimension distinct from the dominant HCHO–NO_2 covariance in the primary three-species axis.

3.5 FNR

The median FNR is 5.60 across the 487 strict matches, with similar medians when only positive HCHO retrievals are retained (5.62) and when NO_2 columns below the 5th or 10th percentile are additionally excluded (5.52 and 5.45), and no significant interannual difference (Kruskal–Wallis H = 0.634, df = 2, p = 0.728). Because the raw distribution is skewed, the median and interquartile range are used rather than the mean; sensitivity to quality-control thresholds is reported in the Supplementary Material (Figure S1). These results support continuous descriptive use of FNR but not categorical classification of ozone-production regimes.

3.6 Hydro-meteorological organization

The 2024–2026 environmental PCA retains 368 observations. PC1 explains 52.2 % of the variance and contrasts Tmax (+0.865) with 7-day antecedent rainfall (−0.733) and RH2M (−0.671), with a positive contribution from solar radiation (+0.593). HCHO covaries positively with this axis (ρ = 0.338). Elevated HCHO is thus associated with a relatively warmer and drier state.

Figure 7 reports Spearman associations between HCHO and the environmental covariates, with 95 % confidence intervals obtained by block bootstrap (L = 7). Tmax is positively associated with HCHO in all three years — ρ = 0.236 (95 % CI −0.047 to 0.461) in 2024, 0.324 (0.108 to 0.461) in 2025, and 0.189 (−0.050 to 0.387) in 2026 — although only the 2025 interval is entirely positive. Seven-day antecedent rainfall is negatively associated with HCHO in all three years: ρ = −0.307 (95 % CI −0.561 to 0.018) in 2024, −0.387 (−0.605 to −0.099) in 2025, and −0.383 (−0.512 to −0.181) in 2026. In 2024 the upper bound lies at the zero boundary (+0.018), so the sign of this association is not robustly established for that year; the intervals are entirely negative in 2025 and 2026. RH2M is negative in all three years, while daily rainfall and solar radiation vary in sign among years; all of these intervals include zero. These covariations are interpreted descriptively with temporal dependence accounted for by the block bootstrap.

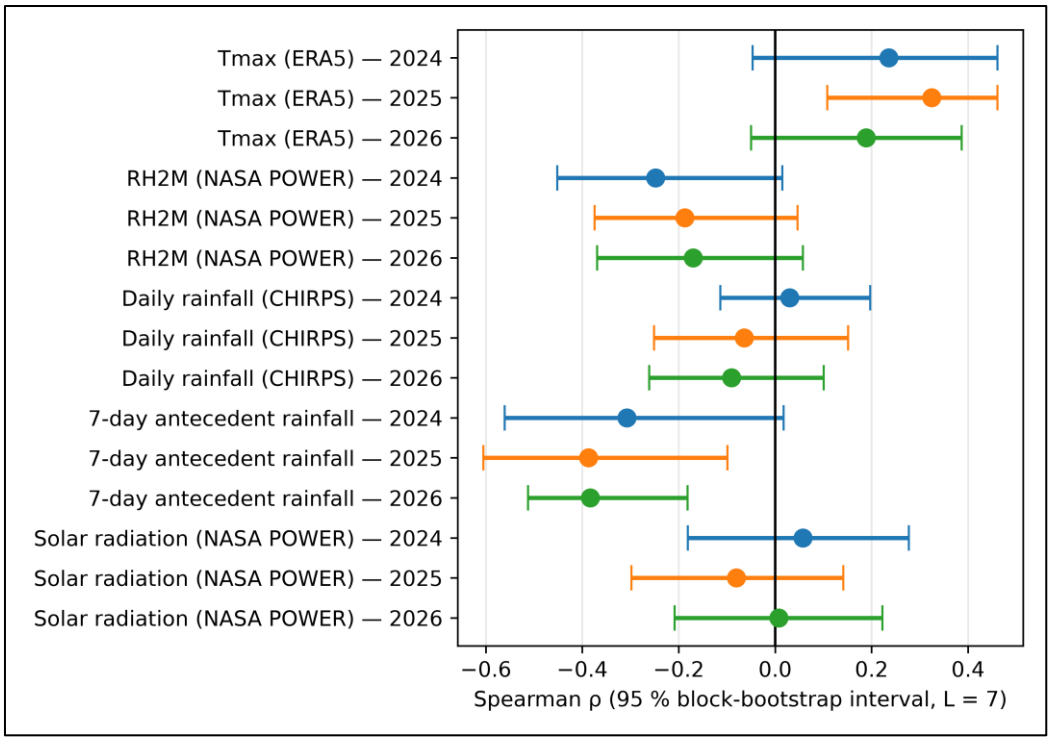


Figure 7: Spearman associations between HCHO and harmonized environmental covariates, accounting for temporal dependence. Points represent observed ρ and bars the 95 % confidence intervals obtained by block bootstrap (L = 7). The panel is retained as environmental context and not as evidence of causality.

3.7 Fires in 2024–2025

The environmental PCA including fires retains 239 observations and explains 58.4 % of the variance on PC1. The dominant loadings are regional FRP +0.922, local FRP +0.859, Tmax +0.852, 7-day antecedent rainfall −0.739, RH2M −0.599, and solar radiation +0.536; HCHO covaries positively with this axis (ρ = 0.356). This organization describes the convergence of high HCHO values with a relatively warm, dry, and more fire-active state during 2024–2025, without constituting causal attribution or an estimate of source contribution.

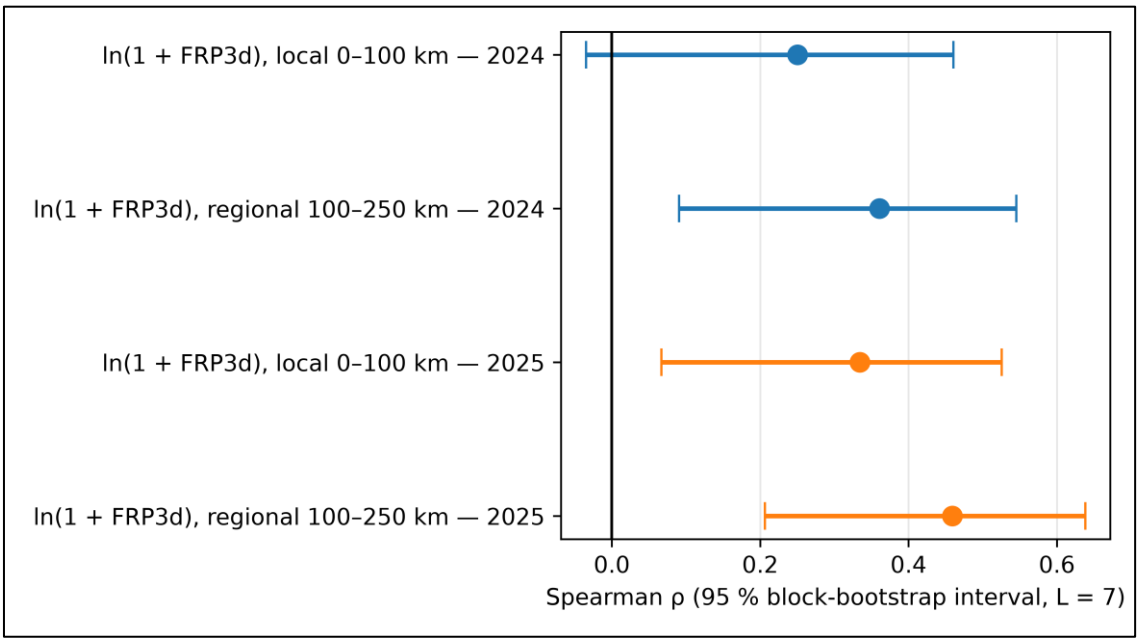


Figure 8: Spearman associations between HCHO and ln(1+FRP3d) for the local (0–100 km) and regional (100–250 km) domains in 2024–2025. Points represent observed ρ and bars the 95 % CIs obtained by block bootstrap (L = 7; 5,000 replications). No 2026 value is shown or imputed.

HCHO–FRP covariance is stronger regionally than locally in both years (Figure 8): in 2024, ρ = 0.250 (95 % CI −0.035 to 0.461) locally and 0.361 (0.091 to 0.545) regionally; in 2025, ρ = 0.334 (0.067 to 0.526) and 0.459 (0.207 to 0.638), respectively. The regional intervals are entirely positive, as is the 2025 local interval, whereas the 2024 local interval includes zero. These coefficients describe covariance, not demonstrated transport or source contribution.

For the 6 February 2024 HYSPLIT–VIIRS pilot, minimum trajectory-to-fire distances within ±1 h were 40.2, 8.0 and 1.8 km at 500, 1000 and 1500 m AGL, respectively. The altitude-dependent coincidence supports transport plausibility for this event only and cannot establish recurrent fire attribution.

3.8 Wind sensitivity

Wind speed was inversely associated with HCHO in 2024 only, and this association did not persist after seasonal adjustment. Because interannual wind coverage is heterogeneous and no homogeneous wind-direction series is available, ventilation is not treated as a demonstrated explanatory mechanism.

3.9 Synthesis of atmospheric-composition patterns

Together, the results identify two contrasting, strongly seasonally structured patterns of atmospheric composition: a relatively HCHO–NO_2-enriched pattern and a chemically attenuated pattern, with CO joining the enriched covariance mode in the complementary five-species analysis. These are descriptive covariance patterns, not source regimes or season-independent physical regimes.

4 DISCUSSION

4.1 Recurrent transition: empirical outcome, scope, and originality

Across 2024–2026, the reproducible result is the direction of a coordinated multipollutant shift rather than an exact calendar date or a unique source: Banco-HCHO shifts from a higher to a lower state and the primary HCHO–NO_2–O_3 axis decreases in the same direction across the estimated transition on the common 441-date support. HCHO–NO_2 covariance remains detectable after categorical seasonal adjustment (ρ = 0.267; Holm-corrected $p = 7.36 \times 10^{-9}$), with block-bootstrap intervals excluding zero at every tested block length, whereas the adjusted HCHO–O_3 association is weakly positive (ρ = +0.069; Holm-corrected p = 0.128) and is not robust at any tested block length. The raw transition decrease persists when HCHO is excluded, although that axis still includes CO and SO_2; independence from the species whose historical extraction chain could not be fully authenticated rests instead on the 487-date composition control, in which standardized NO_2 decreases across the same partitions. The complementary five-species axis shows a broader HCHO–NO_2–CO mode, but categorical seasonal adjustment strongly attenuates its contrast and leaves an interannually variable residual. For the primary axis, no residual contrast is robust under continuous seasonal adjustment (Section 3.4). The contribution of the study is therefore threefold. First, an objectively dated HCHO transition recurs over three consecutive years with overlapping location envelopes and comparable relative decreases (−38.8 % to −44.4 %), all three change points falling within the long rainy season as defined in Section 2.1. Second, NO_2 and the primary HCHO–NO_2–O_3 axis shift in the same direction across these transitions, and the NO_2 control shows that this raw shift is not carried exclusively by HCHO. Third, under a pre-specified harmonic adjustment, no residual component of the primary contrast is robust, whereas the categorical adjustment leaves a robust 2025 residual; this divergence is consistent with transitions that recur at similar calendar dates. A component independent of the seasonal cycle therefore cannot be robustly isolated with the present three-year record, which does not establish that no such component exists. The study thereby delimits what a short satellite record can and cannot resolve at a tropical forest–metropolis interface; it does not constitute source attribution.

Mechanistic attribution remains open: the wind result is not persistent after seasonal adjustment, vertical dilution requires matched boundary-layer-height data, and quantitative separation of biogenic, urban and pyrogenic contributions requires independent source constraints or inverse modelling.

4.2 From the HCHO signal to a multipollutant covariance structure

The primary HCHO–NO_2–O_3 PCA places the HCHO transitions within a documented matched chemical structure, while the no-HCHO and five-species comparisons test dependence on HCHO and added CO/SO_2 covariance. Their common 441-date support shows that the raw transition decrease is not an artefact of variable composition. Seasonal adjustment of the five-species PC1 provides the key qualification: the broader contrast is strongly seasonally structured, with a robust residual in 2025, no robust residual in 2024, and a negative but less robust residual in 2026. These residual patterns derive from categorical adjustment. For the primary axis, the 2025 residual is no longer robust under continuous seasonal adjustment on either support (Section 3.4), so that a season-independent component of the transition cannot be definitively distinguished from the seasonal cycle with the present three-year record. The 2025

residual of the five-species axis, which was not tested under continuous adjustment, is therefore not taken as independent evidence of such a component.

This strategy complements, rather than replaces, source-resolving approaches based on African inversion (Opacka et al., 2025), Chinese satellite assimilation (Feng et al., 2024), European inversion with ground validation (Oomen et al., 2024), and Australasian satellite–ground evaluation (Ryan et al., 2020). In the absence of comparable local inversion and ground infrastructure, Banco contributes three-year replication at a tropical forest–metropolis interface, where biogenic, urban, hydro-meteorological and regional combustion influences can coexist without assuming a dominant source.

4.3 Hydro-meteorological associations

The convergence between HCHO and a warm/dry axis, together with the negative association with antecedent rainfall in all three years (robust in 2025 and 2026), indicates that the chemical organization is closely associated with the hydro-meteorological state. Several mechanisms may contribute to this association—emissions, oxidation, scavenging, transport, and dilution—but the available data do not allow any one mechanism to be isolated quantitatively.

4.4 Wind dispersion: an insufficient explanation

A simple dilution hypothesis would predict that increased ventilation explains a major share of the observed decreases. However, the inverse association with wind speed observed in 2024 does not persist after seasonal adjustment, and coverage is incomplete across years. Wind may contribute to atmospheric organization, but it is not a demonstrated explanation for the transitions here.

4.5 Fires: environmental convergence without attribution

The stronger regional than local HCHO–FRP covariance in both 2024 and 2025 places fire activity within the broader warm/dry environmental context identified here. The targeted HYSPLIT–VIIRS analysis adds event-scale evidence that transport from active-fire regions was physically plausible for one high-HCHO episode, but its single-event design precludes extrapolation to the full record. Fire activity is therefore retained as a plausible regional influence requiring event-resolved transport analysis for stronger attribution.

4.6 NO_2 and CO: strengthening the chemical dimension without source identification

The complementary five-species PCA shows strong NO_2 and CO loadings, but these do not constitute an unambiguous source signature. Because the exact historical extraction chain of the archived CO/SO_2 values is not fully certified, CO and SO_2 are not used to anchor the primary multivariate inference. Their inclusion nevertheless provides complementary evidence that the broader covariance structure extends beyond HCHO, while the primary HCHO–NO_2–O_3 axis retains a negative raw transition-associated contrast in all three years. This compositional comparison is distinct from the seasonal-adjustment sensitivity of the five-species PC1.

4.7 HCHO is not an exclusive biogenic tracer

The immediate proximity of a tropical forest makes a biogenic contribution plausible, but HCHO remains an integrated product of the oxidation of multiple VOCs. In a metropolitan environment, interpretation must simultaneously retain potential contributions from vegetation, urban activities, combustion, and transport. Solar-induced chlorophyll fluorescence (SIF) represents a scientifically relevant, chemically independent vegetation-function proxy that could help test whether HCHO transitions covary with photosynthetic activity.

4.8 O_3: a distinct photochemical context

The weakening of the HCHO–O_3 relationship after categorical seasonal control and the negative O_3 loading on the primary HCHO–NO_2–O_3 PC1 indicate that tropospheric ozone does not simply follow the HCHO–NO_2 covariance axis. This contrast supports an internal organization of atmospheric composition rather than a uniform increase or decrease across all species. The representativeness of a tropospheric O_3 column and its difference from surface ozone are explicitly documented for TROPOMI by Hubert et al. (2021), while the tropospheric ozone context over southern Africa illustrates the interweaving of biomass-burning and anthropogenic influences at the regional scale (Wang et al., 2025).

4.9 FNR as a complementary photochemical indicator

The interannual stability of FNR supports its use here as a complementary descriptor of photochemical context rather than as evidence of a transition between categorical ozone-production regimes. This cautious interpretation is consistent with evidence that meteorology and transport can modify relationships between FNR and ozone (Acdan et al., 2023) and that the FNR values separating ozone-production regimes can vary across urban settings (Jin et al., 2020). Table 3 positions the present study relative to selected regional and international literature.

Table 3: Positioning of the present study relative to selected regional and international literature.

Study / region	Data / approach	Scientific focus	Main relevance / finding	Added value of Banco study
Dhankar and Pani (2025) — Southeast Asia	TROPOMI HCHO with CO, NO_2, LST, precipitation, FRP and EVI	Spatiotemporal HCHO variability and environmental associations	Establishes that HCHO covaries with chemical, meteorological, vegetation and fire indicators in a tropical monsoonal region	Closest thematic comparator; present study moves from the existence of such associations to objectively detected three-year transitions and sensitivity-tested coordinated multipollutant shifts
Opacka et al. (2025) — Africa	TROPOMI HCHO/NO_2 + inverse modelling	VOC and NO_x emission constraints	Source-resolving continental inversion framework	Observational recurrence at a data-sparse forest–metropolis interface
Feng et al. (2024) — China	TROPOMI HCHO + NO_x constraints	NMVOC optimization and ozone impacts	Model-constrained use of satellite HCHO	Empirical covariance robustness without source inversion
Oomen et al. (2024) — Europe	TROPOMI HCHO + inversion + ground validation	Top-down VOC fluxes	Dense validation and inversion infrastructure	Complementary strategy where such infrastructure is unavailable
Ryan et al. (2020) — Australia/New Zealand	TROPOMI + MAX-DOAS/FTIR	HCHO validation and hotspots	Ground-based anchoring of satellite HCHO	Repeated multipollutant transitions and environmental context
Present study — Banco/Abidjan	TROPOMI multipollutants + meteorology + FRP + targeted HYSPLIT	Recurrent HCHO transitions and coordinated multipollutant shifts and their separability from the seasonal cycle, 2024–2026	Three-year recurrence with sensitivity and temporal-dependence tests; residual component not robustly separable from the seasonal cycle under pre-specified harmonic adjustment	Anchors primary PCA to the HCHO–NO_2–O_3 photochemical block; retains five-species PCA as complementary context; integrates hydro-meteorology, fire covariance, and bounded transport feasibility

5 CONCLUSIONS

The Banco forest–metropolis interface exhibits a recurrent 2024–2026 HCHO transition, objectively dated on 9 March 2024, 13 April 2025 and 13 April 2026, accompanied by strongly seasonally structured coordinated multipollutant shifts. On 441 five-species complete-case dates, the primary HCHO–NO_2–O_3 PC1 explains 54.1 % of variance and has raw transition contrasts of −1.416, −1.737 and −1.368; the loading pattern, contrast direction and seasonal structuring are preserved on the full 487-date population. After categorical seasonal adjustment, the primary residual contrasts are +0.026, −0.409 and −0.188; the residual decrease is robust across all tested block lengths only in 2025, while the 2024 and 2026 intervals include zero. Under a pre-specified continuous seasonal adjustment, however, no primary residual contrast satisfies the robustness criterion in any year, on either support or under any tested variant, whereas the raw contrasts remain robust on both supports. The primary multivariate transition is therefore strongly seasonally structured; its residual component depends on how seasonality is represented, and a season-independent component of the transition cannot be definitively distinguished from the seasonal cycle. The divergence between the categorical and harmonic representations is consistent with transitions that recur at similar calendar dates, and the absence of a robust residual does not establish that no season-independent component exists. The complementary five-species analysis shows that CO joins the dominant HCHO–NO_2 covariance mode but is not required for the primary inference.

Five-species ΔPC1 values of −1.987, −2.528 and −1.839 are strongly attenuated after categorical seasonal adjustment to −0.087, −0.941 and −0.394; the residual is not robust in 2024, robust in 2025, and negative but not uniformly robust in 2026. This complementary residual was evaluated under categorical adjustment only. HCHO–NO_2 remains detectable

after categorical seasonal adjustment, whereas the weak HCHO–O_3 anticorrelation does not. Standardized NO_2, which contains no HCHO and requires neither CO nor SO_2, decreases robustly across the same partitions in all three years before seasonal adjustment, so the raw shift is not carried exclusively by HCHO.

The exhaustive circular-shift randomization further shows that the five-species transition contrasts occupy extreme ranks among the admissible circular shifts of that axis, without establishing independence from seasonality.

The seasonally structured coordinated multipollutant shifts are associated with relatively warm/dry versus more humid conditions; in 2024–2025, fire activity also covaries with the warm/dry pattern and HCHO. A single-event HYSPLIT–VIIRS pilot supports transport plausibility but not recurrent pyrogenic attribution. These contrasting atmospheric-composition patterns remain descriptive and are not equated with source regimes or season-independent physical regimes.

Future work should prioritize event-resolved transport and boundary-layer constraints, together with source-resolving inversion and independent ground-based validation. Extending HYSPLIT to objective high- and low-HCHO event samples and matching PBLH observations to the Banco record would better constrain transport and vertical dilution, while joint HCHO–NO_2 inversion, potentially extended to glyoxal, and MAX-DOAS or Pandora observations could provide stronger source and local observational constraints (De Smedt et al., 2021; Hubert et al., 2021; Opacka et al., 2025; Sfendla et al., 2026).

Limitations

The integration of satellite, reanalysis, meteorological and fire products involves differences in spatial, temporal and vertical representativeness. Tropospheric O_3 characterizes the regional photochemical context rather than surface ozone. The historical extraction documentation is incomplete for the O_3 extraction settings and the original multi-gas script, and CO and SO_2, whose values could not be authenticated against an archived export, are restricted to complementary analyses ((Section 2.3 and Data availability and reproducibility). The absence of matched daily PBLH and SIF observations precludes direct quantification of vertical mixing and vegetation activity. Without a paired non-forest control site, the observed transitions are interpreted as associations rather than as effects of the forest. The common 1 January–8 August window (the 2026 record ending on 8 August) ensures interannual comparability but excludes the short rainy season (September–November).

Seasonal adjustment is the main source of inferential sensitivity, particularly for the 2025 primary-axis residual, which is robust under the categorical three-season adjustment but not under the continuous harmonic adjustment. Because the transitions recur at similar calendar dates, a smooth seasonal cycle can absorb part of the transition, whereas a fixed partition may leave part of the seasonal cycle in the residual; the three-year record does not favour either reading, so no season-independent component is claimed. The five-species residual contrasts, categorically adjusted correlations and composition controls were assessed under categorical adjustment only.

STATEMENTS ON COMPLIANCE WITH ETHICAL STANDARDS

Acknowledgments

The authors acknowledge the European Space Agency (ESA) and the Copernicus programme for Sentinel-5P/TROPOMI atmospheric composition products; the European Centre for Medium-Range Weather Forecasts (ECMWF) for ERA5; the NASA POWER project for meteorological and surface-radiation data; the Climate Hazards Center for CHIRPS precipitation data; and NASA FIRMS for access to VIIRS active-fire observations. Google Earth Engine is acknowledged as the cloud-processing environment used for satellite-data access and reproducibility workflows. These acknowledgements refer only to products and platforms actually used in the analyses.

Disclosure of conflict of interest

The authors declare that they have no known competing financial interests or personal relationships that could have appeared to influence the work reported in this paper.

Author contributions

Aka Jacques Adon: Conceptualization; Writing – original draft. Guebi Daniel Akagbo: Conceptualization; Writing – original draft. Véronique Yoboué: Conceptualization; Writing – review &. Editing. Aristide Akpo: Writing – review & editing.

Data availability and reproducibility

The source datasets (Sentinel-5P/TROPOMI, ERA5, NASA POWER, CHIRPS and VIIRS/S-NPP) are accessible from their respective providers. Two certified analytical datasets and five accompanying workbooks document the inputs, parameters and sensitivity tests of the statistical analyses; executable code is retained for the continuous seasonal-adjustment sensitivity. Some upstream steps could not be recovered: the historical CO/SO_2 export, the tropospheric O_3 extraction settings, the VIIRS processing to daily FRP, the VIIRS extraction of the HYSPLIT pilot and the wind sensitivity analysis; the corresponding values are retained as reported. The retained material may be obtained from the corresponding author upon reasonable request, subject to the licensing terms of the source products; unrecovered materials are excluded.

REFERENCES

[1] Acdan, J. J. M., Pierce, R. B., Dickens, A. F., Adelman, Z., & Nergui, T. (2023). Examining TROPOMI formaldehyde to nitrogen dioxide ratios in the Lake Michigan region: implications for ozone exceedances. Atmospheric Chemistry and Physics, 23, 7867–7885. https://doi.org/10.5194/acp-23-7867-2023.

[2] Adon, A. J., Liousse, C., Doumbia, E. T., Baeza-Squiban, A., Cachier, H., Léon, J.-F., Yoboué, V., Akpo, A. B., Galy-Lacaux, C., Guinot, B., Zouiten, C., Xu, H., Gardrat, E., & Keita, S. (2020). Physico-chemical characterization of urban aerosols from specific combustion sources in West Africa at Abidjan in Côte d'Ivoire and Cotonou in Benin in the frame of the DACCIWA program. Atmospheric Chemistry and Physics, 20, 5327–5354. https://doi.org/10.5194/acp-20-5327-2020.

[3] De Smedt, I., Pinardi, G., Vigouroux, C., Compernolle, S., Bais, A., Benavent, N., Boersma, F., Chan, K.-L., Donner, S., Eichmann, K.-U., Hedelt, P., Hendrick, F., Irie, H., Kumar, V., Lambert, J.-C., Langerock, B., Lerot, C., Liu, C., Loyola, D., Piters, A., Richter, A., Rivera Cárdenas, C., Romahn, F., Ryan, R. G., Sinha, V., Theys, N., Vlietinck, J., Wagner, T., Wang, T., Yu, H., & Van Roozendael, M. (2021). Comparative assessment of TROPOMI and OMI formaldehyde observations and validation against MAX-DOAS network column measurements. Atmospheric Chemistry and Physics, 21, 12561–12593. https://doi.org/10.5194/acp-21-12561-2021.

[4] Dhankar, S., & Pani, B. (2025). Spatio-temporal analysis of formaldehyde and its association with atmospheric and environmental variables over the Southeast Asian region using satellite data. Environmental Monitoring and Assessment, 197, 185. https://doi.org/10.1007/s10661-025-13617-2.

[5] Feng, S., Jiang, F., Qian, T., Wang, N., Jia, M., Zheng, S., Chen, J., Ying, F., & Ju, W. (2024). Constraining non-methane VOC emissions with TROPOMI HCHO observations: impact on summertime ozone simulation in August 2022 in China. Atmospheric Chemistry and Physics, 24, 7481–7498. https://doi.org/10.5194/acp-24-7481-2024.

[6] Funk, C., Peterson, P., Landsfeld, M., Pedreros, D., Verdin, J., Shukla, S., Husak, G., Rowland, J., Harrison, L., Hoell, A., & Michaelsen, J. (2015). The climate hazards infrared precipitation with stations—a new environmental record for monitoring extremes. Scientific Data, 2, 150066. https://doi.org/10.1038/sdata.2015.66.

[7] Guenther, A. B., Jiang, X., Heald, C. L., Sakulyanontvittaya, T., Duhl, T., Emmons, L. K., & Wang, X. (2012). The Model of Emissions of Gases and Aerosols from Nature version 2.1 (MEGAN2.1): an extended and updated framework for modeling biogenic emissions. Geoscientific Model Development, 5, 1471–1492. https://doi.org/10.5194/gmd-5-1471-2012.

[8] Hersbach, H., Bell, B., Berrisford, P., Hirahara, S., Horányi, A., Muñoz-Sabater, J., Nicolas, J., Peubey, C., Radu, R., Schepers, D., Simmons, A., Soci, C., Abdalla, S., Abellan, X., Balsamo, G., Bechtold, P., Biavati, G., Bidlot, J., Bonavita, M., De Chiara, G., Dahlgren, P., Dee, D. P., Diamantakis, M., Dragani, R., Flemming, J., Forbes, R., Fuentes, M., Geer, A. J., Haimberger, L., Healy, S. B., Hogan, R. J., Hólm, E., Janisková, M., Keeley, S., Laloyaux, P., Lopez, P., Lupu, C., Radnoti, G., de Rosnay, P., Rozum, I., Vamborg, F., Villaume, S., & Thépaut, J.-N. (2020). The ERA5 global reanalysis. Quarterly Journal of the Royal Meteorological Society, 146, 1999–2049. https://doi.org/10.1002/qj.3803.

[9] Holm, S. (1979). A simple sequentially rejective multiple test procedure. Scandinavian Journal of Statistics, 6, 65–70.

[10] Hubert, D., Heue, K.-P., Lambert, J.-C., Verhoelst, T., Allaart, M., Compernolle, S., Cullis, P. D., Dehn, A., Félix, C., Johnson, B. J., Keppens, A., Kollonige, D. E., Lerot, C., Loyola, D., Maata, M., Mitro, S., Mohamad, M., Piters, A., Romahn, F., Selkirk, H. B., da Silva, F. R., Stauffer, R. M., Thompson, A. M., Veefkind, J. P., Vömel, H., Witte, J. C., & Zehner, C. (2021). TROPOMI tropospheric ozone column data: geophysical assessment and comparison to ozonesondes, GOME-2B and OMI. Atmospheric Measurement Techniques, 14, 7405–7433. https://doi.org/10.5194/amt-14-7405-2021.

[11] Jin, X., Fiore, A. M., Boersma, K. F., De Smedt, I., & Valin, L. (2020). Inferring changes in summertime surface ozone–NO_x–VOC chemistry over U.S. urban areas from two decades of satellite and ground-based observations. Environmental Science & Technology, 54, 6518–6529. https://doi.org/10.1021/acs.est.9b07785.

[12] Johnson, M. S., Souri, A. H., Philip, S., Kumar, R., Naeger, A., Geddes, J., Judd, L., Janz, S., Chong, H., & Sullivan, J. (2023). Satellite remote-sensing capability to assess tropospheric-column ratios of formaldehyde and nitrogen dioxide: case study during the Long Island Sound Tropospheric Ozone Study 2018 (LISTOS 2018) field campaign. Atmospheric Measurement Techniques, 16, 2431–2454. https://doi.org/10.5194/amt-16-2431-2023.

[13] Jolliffe, I. T., & Cadima, J. (2016). Principal component analysis: a review and recent developments. Philosophical Transactions of the Royal Society A, 374, 20150202. https://doi.org/10.1098/rsta.2015.0202.

[14] Knippertz, P., Coe, H., Chiu, J. C., Evans, M. J., Fink, A. H., Kalthoff, N., Liousse, C., Mari, C., Allan, R. P., Brooks, B., Danour, S., Flamant, C., Jegede, O. O., Lohou, F., & Marsham, J. H. (2015). The DACCIWA Project: Dynamics–Aerosol–Chemistry–Cloud Interactions in West Africa. Bulletin of the American Meteorological Society, 96, 1451–1460. https://doi.org/10.1175/BAMS-D-14-00108.1.

[15] Kruskal, W. H., & Wallis, W. A. (1952). Use of ranks in one-criterion variance analysis. Journal of the American Statistical Association, 47, 583–621. https://doi.org/10.1080/01621459.1952.10483441.

[16] Marais, E. A., Jacob, D. J., Kurosu, T. P., Chance, K., Murphy, J. G., Reeves, C., Mills, G., Casadio, S., Millet, D. B., Barkley, M. P., Paulot, F., & Mao, J. (2012). Isoprene emissions in Africa inferred from OMI observations of formaldehyde columns. Atmospheric Chemistry and Physics, 12, 6219–6235. https://doi.org/10.5194/acp-12-6219-2012.

[17] Monks, P. S., Archibald, A. T., Colette, A., Cooper, O., Coyle, M., Derwent, R., Fowler, D., Granier, C., Law, K. S., Mills, G. E., Stevenson, D. S., Tarasova, O., Thouret, V., von Schneidemesser, E., Sommariva, R., Wild, O., & Williams, M. L. (2015). Tropospheric ozone and its precursors from the urban to the global scale from air quality to short-lived climate forcer. Atmospheric Chemistry and Physics, 15, 8889–8973. https://doi.org/10.5194/acp-15-8889-2015.

[18] Oomen, G.-M., Müller, J.-F., Stavrakou, T., De Smedt, I., Blumenstock, T., Kivi, R., Makarova, M., Palm, M., Röhling, A., Té, Y., Vigouroux, C., Friedrich, M. M., Frieß, U., Hendrick, F., Merlaud, A., Piters, A., Richter, A., Van Roozendael, M., & Wagner, T. (2024). Weekly derived top-down volatile-organic-compound fluxes over Europe from TROPOMI HCHO data from 2018 to 2021. Atmospheric Chemistry and Physics, 24, 449–474. https://doi.org/10.5194/acp-24-449-2024.

[19] Opacka, B., Stavrakou, T., Müller, J.-F., De Smedt, I., van Geffen, J., Marais, E. A., Horner, R. P., Millet, D. B., Wells, K. C., & Guenther, A. B. (2025). Natural emissions of VOC and NO_x over Africa constrained by TROPOMI HCHO and NO_2 data using the MAGRITTEv1.1 model. Atmospheric Chemistry and Physics, 25, 2863–2894. https://doi.org/10.5194/acp-25-2863-2025.

[20] Pettitt, A. N. (1979). A non-parametric approach to the change-point problem. Applied Statistics, 28, 126–135. https://doi.org/10.2307/2346729.

[21] Ryan, R. G., Silver, J. D., Querel, R., Smale, D., Rhodes, S., Tully, M., Jones, N., & Schofield, R. (2020). Comparison of formaldehyde tropospheric columns in Australia and New Zealand using MAX-DOAS, FTIR and TROPOMI. Atmospheric Measurement Techniques, 13, 6501–6519. https://doi.org/10.5194/amt-13-6501-2020.

[22] Schroeder, J. R., Crawford, J. H., Fried, A., Walega, J., Weinheimer, A., Wisthaler, A., Müller, M., Mikoviny, T., Chen, G., Shook, M., Blake, D. R., & Tonnesen, G. S. (2017). New insights into the column $CH2O/NO_2$ ratio as an indicator of near-surface ozone sensitivity. Journal of Geophysical Research: Atmospheres, 122, 8885–8907. https://doi.org/10.1002/2017JD026781.

[23] Schroeder, W., Oliva, P., Giglio, L., & Csiszar, I. A. (2014). The new VIIRS 375 m active fire detection data product: algorithm description and initial assessment. Remote Sensing of Environment, 143, 85–96. https://doi.org/10.1016/j.rse.2013.12.008.

[24] Sfendla, Y., Stavrakou, T., Müller, J.-F., Oomen, G.-M., Opacka, B., Danckaert, T., De Smedt, I., & Lerot, C. (2026). Global VOC emissions quantified from inversion of TROPOMI spaceborne formaldehyde and glyoxal data. Atmospheric Chemistry and Physics, 26, 733–767. https://doi.org/10.5194/acp-26-733-2026.

[25] Souri, A. H., González Abad, G., Duncan, B. N., & Oman, L. D. (2026). Beyond binary maps from $HCHO/NO_2$: a deep neural network approach to global daily mapping of net ozone production rates and sensitivities constrained by satellite observations (2005–2023). Atmospheric Chemistry and Physics, 26, 809–837. https://doi.org/10.5194/acp-26-809-2026.

[26] Souri, A. H., Johnson, M. S., Wolfe, G. M., Crawford, J. H., Fried, A., Wisthaler, A., Brune, W. H., Blake, D. R., Weinheimer, A. J., Verhoelst, T., Compernolle, S., Pinardi, G., Vigouroux, C., Langerock, B., Choi, S., Lamsal, L., Zhu, L., Sun, S., Cohen, R. C., Min, K.-E., Cho, C., Philip, S., Liu, X., & Chance, K. (2023). Characterization of errors in satellite-based $HCHO/NO_2$ tropospheric column ratios with respect to chemistry, column-to-PBL translation, spatial representation, and retrieval uncertainties. Atmospheric Chemistry and Physics, 23, 1963–1986. https://doi.org/10.5194/acp-23-1963-2023.

[27] Tian, Y., Wang, S., & Jin, X. (2025). Global patterns and trends in ground-level ozone chemical formation regimes from 1996 to 2022. Atmospheric Chemistry and Physics, 25, 9127–9149. https://doi.org/10.5194/acp-25-9127-2025.

[28] van Geffen, J., Eskes, H., Compernolle, S., Pinardi, G., Verhoelst, T., Lambert, J.-C., Sneep, M., ter Linden, M., Ludewig, A., Boersma, K. F., & Veefkind, J. P. (2022). Sentinel-5P TROPOMI NO_2 retrieval: impact of version v2.2 improvements and comparisons with OMI and ground-based data. Atmospheric Measurement Techniques, 15, 2037–2060. https://doi.org/10.5194/amt-15-2037-2022.

[29] Veefkind, J. P., Aben, I., McMullan, K., Förster, H., de Vries, J., Otter, G., Claas, J., Eskes, H. J., de Haan, J. F., Kleipool, Q., van Weele, M., Hasekamp, O., Hoogeveen, R., Landgraf, J., Snel, R., Tol, P., Ingmann, P., Voors, R., Kruizinga, B., Vink, R., Visser, H., & Levelt, P. F. (2012). TROPOMI on the ESA Sentinel-5 Precursor: a GMES mission for global observations of the atmospheric composition for climate, air quality and ozone layer applications. Remote Sensing of Environment, 120, 70–83. https://doi.org/10.1016/j.rse.2011.09.027.

[30] Wang, Y., Li, K., Chen, X., Yang, Z., Tang, M., Campos, P. M. D., Yang, Y., Yue, X., & Liao, H. (2025). Revisiting the high tropospheric ozone over southern Africa: role of biomass burning and anthropogenic emissions. Atmospheric Chemistry and Physics, 25, 4455–4475. https://doi.org/10.5194/acp-25-4455-2025.